OPEN ACCESS
IOP Publishing
Semiconductor Science and Technology
Semicond. Sci. Technol. **35** (2020) 054001 (15pp)
https://doi.org/10.1088/1361-6641/ab75a5

Structural and luminescence imaging and characterisation of semiconductors in the scanning electron microscope

C Trager-Cowan[1], A Alasmari[1], W Avis[1], J Bruckbauer[1], P R Edwards[1], G Ferenczi[1], B Hourahine[1], A Kotzai[1], S Kraeusel[1], G Kusch[1], R W Martin[1], R McDermott[1], G Naresh-Kumar[1], M Nouf-Allehiani[1], E Pascal[1], D Thomson[1], S Vespucci[1], M D Smith[2], P J Parbrook[2], J Enslin[3], F Mehnke[3], C Kuhn[3], T Wernicke[3], M Kneissl[3,4], S Hagedorn[4], A Knauer[4], S Walde[4], M Weyers[4], P-M Coulon[5], P A Shields[5], J Bai[6], Y Gong[6], L Jiu[6], Y Zhang[6], R M Smith[6], T Wang[6] and A Winkelmann[1,7]

[1] Department of Physics, SUPA, University of Strathclyde, Glasgow, G4 0NG, United Kingdom
[2] Tyndall National Institute, University College Cork, Cork, T12 R5CP, Ireland
[3] Institut für Festkörperphysik, Technische Universität Berlin, D-10623 Berlin, Germany
[4] Ferdinand-Braun-Institut, Leibniz-Institut für Höchstfrequenztechnik, D-12489 Berlin, Germany
[5] Department of Electronic and Electrical Engineering, University of Bath, Bath, BA2 7AY, United Kingdom
[6] Department of Electronic and Electrical Engineering, University of Sheffield, Sheffield, S1 3JD, United Kingdom
[7] Academic Centre for Materials and Nanotechnology (ACMiN), AGH University of Science and Technology, Krakow, Poland

E-mail: c.trager-cowan@strath.ac.uk

Received 2 September 2019, revised 30 January 2020
Accepted for publication 12 February 2020
Published 25 March 2020

Abstract

The scanning electron microscopy techniques of electron backscatter diffraction (EBSD), electron channelling contrast imaging (ECCI) and cathodoluminescence (CL) hyperspectral imaging provide complementary information on the structural and luminescence properties of materials rapidly and non-destructively, with a spatial resolution of tens of nanometres. EBSD provides crystal orientation, crystal phase and strain analysis, whilst ECCI is used to determine the planar distribution of extended defects over a large area of a given sample. CL reveals the influence of crystal structure, composition and strain on intrinsic luminescence and/or reveals defect-related luminescence. Dark features are also observed in CL images where carrier recombination at defects is non-radiative. The combination of these techniques is a powerful approach to clarifying the role of crystallography and extended defects on a material's light emission properties. Here we describe the EBSD, ECCI and CL techniques and illustrate their use for investigating the structural and light emitting properties of UV-emitting nitride semiconductor structures. We discuss our investigations of the type, density and distribution of defects in GaN, AlN and AlGaN thin films and also discuss the determination of the polarity of GaN nanowires.

Keywords: SEM, EBSD, CL, ECCI, nitride, extended defects

(Some figures may appear in colour only in the online journal)

1. Introduction

The scanning electron microscope (SEM) is a very powerful tool for investigating and imaging a wide range of material properties spanning topography, structure, composition and light emission [1–4]. SEMs are extensively used for imaging topography by monitoring the intensity of secondary electrons as a focussed electron beam, with an energy in the range of 100 eV to 30 keV, is rastered over the surface of a sample. Less well known are the techniques of electron channelling contrast imaging (ECCI) [5–12] and electron backscatter diffraction (EBSD) [5, 6, 13, 14] which exploit diffraction to provide information on crystal structure, crystal misorientation, grain boundaries, strain and extended defects such as dislocations and stacking faults. Cathodoluminescence (CL), that is light emission generated when an electron beam is incident on a sample, provides valuable information on a sample's luminescence properties [15–17]. CL can reveal the influence of crystal structure, composition and strain on intrinsic luminescence and/or defect-related luminescence. Dark features are also observed where carrier recombination at defects is non-radiative. The combination of EBSD, ECCI and CL is a powerful tool for clarifying the role of crystallography and extended defects on a material's light emission properties.

In this article we describe the SEM techniques of EBSD, ECCI and CL hyperspectral imaging and illustrate the capability of each technique for the characterisation of semiconductors. To this end we present our recent results on the use of these non-destructive techniques to obtain information on the topography, crystal misorientation, defect distributions and light emission from a range of UV emitting nitride (Al(Ga)N-based) semiconductor structures. We also give examples where combining these techniques can provide useful complementary information.

In comparison to their visible cousins, UV light emitting diodes (LEDs) based on nitride semiconductor thin films exhibit poor optoelectronic properties with external quantum efficiencies typically no more than 10% for wavelengths less than 350 nm [18]. Their ultimate performance is presently limited by the structural quality of AlN and AlGaN thin films, which limits the achievable internal quantum efficiency (IQE), and by low doping efficiencies, low carrier injection efficiencies and poor light extraction [19]. Key to improving the performance of UV LEDs, and the main motivation for the research described in this paper, is the understanding and control of extended defects such as grain boundaries, threading dislocations (TDs), partial dislocations and stacking faults and their influence on light emission for Al(Ga)N-based semiconductors.

To carry out our measurements we use a range of SEMs equipped with both commercial and bespoke detection systems. In the work reported here we have used an FEI Sirion 200 Schottky field emission gun SEM (Sirion SEM) equipped with an in-house developed ECCI system. We have also used an FEI Quanta 250 Schottky field emission gun environmental/variable pressure SEM (Quanta SEM) equipped with gaseous electron detectors for electron detection when the SEM is used in low vacuum and environmental modes. The Quanta SEM is also equipped with an Oxford Instruments Nordlys EBSD detector and forescatter diodes for EBSD and ECCI measurements respectively, and an in-house developed CL hyperspectral imaging system. The CL system utilizes a Schwarzschild reflecting objective to collect the emission from a sample inclined at 45°, allowing the collection of light with wavelengths $\geqslant$200 nm. The ability to vary the pressure in the chamber of the Quanta SEM allows the dissipation of charge and therefore imaging of high resistivity materials such as AlGaN and AlN. Sections 2 and 3 summarise the ECCI, EBSD and CL techniques and outline the equipment specifications required to produce the results presented.

2. The ECCI and EBSD techniques

ECCI and EBSD both exploit diffraction to reveal the structural properties of the crystalline material under investigation. For ECCI it is diffraction of the incident beam which provides the greatest contrast in the resultant images, while for EBSD it is diffraction of backscattered electrons which provides the crystallographic information. The spatial and depth resolution of both techniques is of the order of tens of nanometres. For successful imaging using either ECCI or EBSD, the sample needs to have a reasonably smooth and clean surface. For the imaging of metal surfaces or the surfaces of geological specimens, this usually requires careful sample polishing to produce a high quality surface [10], this is also the case for semiconductor wafers cut from bulk crystals. Samples are typically mechanically polished to an optical finish using standard metallographic techniques, grinding with successively finer diamond grit and finishing with a 20 min colloidal silica polish as the final stage. Samples can also be further polished using an argon ion beam polishing system to remove any fine scratches due to the mechanical polishing [10, 20, 21]. However, for most epitaxially grown semiconductor thin films, no surface preparation is required.

2.1. Electron channelling contrast imaging (ECCI)

ECCI micrographs may be produced when a sample is placed so that a plane or planes are at, or close to, their Bragg angle with respect to the incident electron beam. Any deviation in crystallographic orientation or in lattice constant due to local strain will produce a variation in contrast in the resultant ECCI micrograph. This is because diffraction of the incident beam changes the intensity of the backscattered electrons

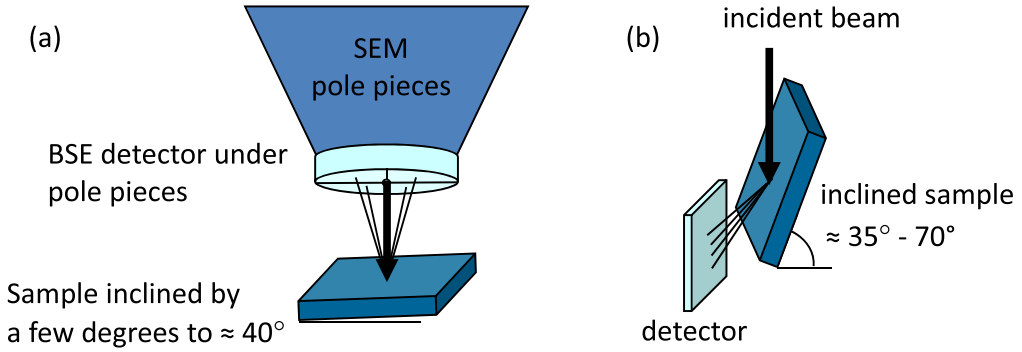

Figure 1. Illustration of the (a) backscatter and (b) forescatter geometries for acquisition of ECCI micrographs. Reproduced with permission from [31]. © 2019 The Institution of Engineering and Technology.

compared to when no diffraction occurs. A change in orientation or lattice constant changes the diffraction conditions; this results in a change in the intensity of the backscattered electrons. The ECCI micrograph is constructed by monitoring the intensity of backscattered or forescattered electrons as the electron beam is scanned over the sample. Extremely small changes in orientation and strain are detectable, revealing, for example, low angle tilt and rotation boundaries and atomic steps. Extended defects such as dislocations and stacking faults may also be imaged [5–12, 22–27]. The conditions required to resolve individual dislocations in an electron channelling contrast image are quite stringent; a small (nanometres), high brightness (nanoamps or higher), low divergence (a few mrad) electron beam is required [5, 28]. Such conditions are met in a field emission gun SEM. The ECCI micrographs shown in this paper were acquired at either 25 or 30 keV, and we show ECCI micrographs where dislocations of order 80 nm apart can be resolved. ECCI micrographs can be acquired at lower electron beam energies, for example see [29, 30]. In [29] the smallest size of the investigated 3D structures revealed in their ECCI micrographs was 28 nm.

Figure 1 illustrates the two geometries, namely the backscatter and forescatter geometries which are used to acquire ECCI micrographs. The backscatter geometry (figure 1(a)) has the advantage that this geometry does not require a high tilt of the sample and therefore no significant correction of the image to account for tilt is required. This geometry also allows the easiest imaging of large samples, for example full semiconductor wafers. The forescatter geometry (figure 1(b)) has the advantage that images exhibit better signal-to-noise compared to the backscatter geometry, due to the increase in intensity of backscattered electrons. The detector used to detect the backscattered electrons is generally an electron-sensitive diode. Vital to the acquisition of good quality ECCI micrographs is the use of a good amplification system. An amplifier with a large DC offset and high small signal gain greatly facilitates the acquisition of ECCI micrographs. To obtain the signal to noise displayed in the ECCI micrographs shown in this paper, images with ≈4 million pixels were acquired with acquisition times of 30–100 s. Frame averaging was also used as required, increasing image acquisition time to a few minutes.

Key to the interpretation of ECCI micrographs, in particular for identification of observed extended defects, is knowledge of the diffraction condition at which the ECCI micrograph was acquired, i.e. knowing which plane diffracted the incident electron beam. Determining/selection of the diffracting plane(s) may be achieved by acquiring electron channelling patterns (ECPs), this is discussed in the following section.

2.2. Selection/determination of the diffraction condition for ECCI, acquiring ECPs

An ECP is obtained when changes in the backscattered electron intensity are recorded as the angle of the incident electron beam is changed relative to the surface of a single crystal area of the sample. When the beam changes its angle with respect to the sample, different planes of the crystal satisfy the Bragg condition, giving rise to the appearance of overlapping bands, known as Kikuchi bands, superimposed on the image of the sample. An ECP from a GaN thin film is shown in figure 2. The ECP is closely related to the 2D projection of the crystal structure, with the Kikuchi bands corresponding to different planes in the crystal. Comparing the ECP with kinematical and/or dynamical electron diffraction simulations allows the pattern to be indexed, i.e. the planes in the ECP can be identified. The plane (or planes) which intersect the centre of the ECP, usually referred to as the pattern centre (PC), are those from which the incident electron beam is diffracted. In the example shown in figure 2, the incident electron beam was diffracted from one of the {11-20} planes; so the **g**-vector, the vector normal to the diffracting plane, is one of {11-20}.

An ECP may be obtained by acquiring a backscattered image at low magnification. At low magnification, as the beam is scanned over the sample, it changes its angle with respect to the surface of the sample (in our case, for our Sirion SEM, this is by around ±2.5°), allowing an ECP to be obtained [9]. Note that this method of acquiring an ECP is only possible if the scanned area of the sample (of order 5 mm × 5 mm in size) is smooth and all of the same crystallographic orientation. An ECCI micrograph is obtained on zooming in on the PC by increasing the magnification. At higher magnification the beam nominally has a fixed angle

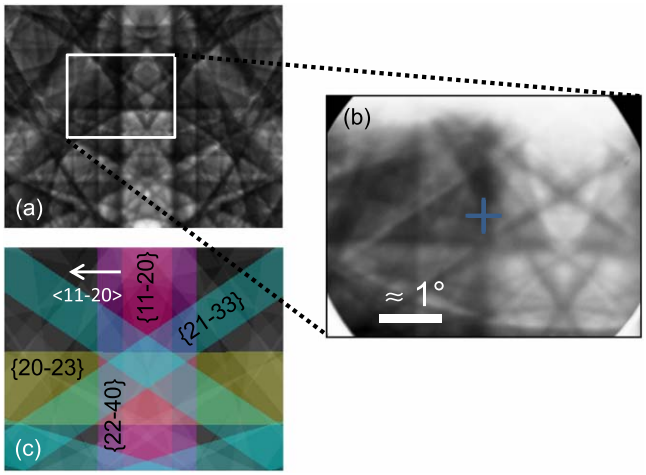

Figure 2. (a) Dynamical simulation of an electron channelling pattern (ECP) from a GaN thin film. Electron beam energy is 30 keV, sample tilt ≈40°. (b) Experimental ECP. The blue cross marks the pattern centre (PC). (c) Kinematical simulation of the ECP with some indexed planes highlighted (produced with ESPRIT DynamicS (Bruker Nano) software). In this case the PC intersects with the edge of one of the {11-20} Kikuchi bands; so the **g**-vector is one of {11-20}. Reproduced with permission from [31]. © 2019 The Institution of Engineering and Technology.

with respect to the sample surface as the beam is scanned. The resultant ECCI micrograph will reveal any defects which distort the plane or planes which correspond to the Kikuchi bands intersecting the PC. Alternatively, if 'beam rocking' electron optics are available in the SEM, the angle of the beam with respect to the sample can be changed over a much smaller surface area. Selected area ECPs, referred to as SAECPS or SACPs can be acquired from areas ranging from a 10 μm × 10 μm down to of around 500 nm × 500 nm in size [32]. Moreover with 'beam rocking', ECPs can also be acquired for a larger angular range, up to of order ±10° [8]. While a lot of useful information can be obtained from ECCI without the acquisition of ECPs, the ability to acquire ECPs makes ECCI far more powerful and easier to use. The ability to select the diffraction condition is particularly useful when applying ECCI to the identification of unknown extended defects such as dislocations and stacking faults. How the knowledge of the **g**-vector may be applied to the identification of dislocations is discussed in section 4.1.

2.3. Electron backscatter diffraction (EBSD)

In EBSD the sample is tilted at around 70° to the normal of the incident electron beam. The impinging electrons are scattered inelastically through high angles forming a diverging source of electrons which can be diffracted. The resultant electron backscatter pattern (EBSP) consists of a large number of overlapping Kikuchi bands. An EBSP, like an ECP (the two are related by reciprocity) is closely related to a 2D projection of the crystal structure, where each Kikuchi band corresponds to a set of planes, as illustrated in figure 3(b). An EBSP generally spans a greater angular range than an ECP. EBSPs are generally detected by an electron sensitive phosphor or scintillator screen and a charge-coupled device or complementary metal-oxide semiconductor camera [13] (see figure 3(a)), although there have been recent developments of direct electron cameras [33, 34]. The spatial resolution achievable in an EBSD map is of order 100 nm [35, 36]. The EBSP shown in figure 3(b) was acquired at 20 keV from a Si sample using energy-filtered direct electron detection with a collection angle of ≈50°. Direct electron detection allows high quality EBSPs to be acquired at low electron beam energies, pattern acquisition down to 3 keV is achievable [28]. Acquisition of EBSD maps at lower electron beam energy should lead to higher spatial resolution [35]. EBSD is a well-established technique for texture analysis and for quantifying grain boundaries and crystal phases [5, 6, 13, 14]. The introduction of cross-correlation based analysis of EBSPs has improved the measurement precision of relative orientation with rotations of 0.01° measurable. For measurement of strain, strain changes of order 2×10^{-4} have been resolved. Such precise measurements of relative orientation and strain have allowed the determination of geometrically necessary dislocation densities [14, 37]. Cross-correlation of experimental patterns with dynamical simulations have enabled the mapping of antiphase domains [38] and crystal polarity [39, 40]. Using the technique described in [35], the spatial resolution exhibited by the EBSD maps in the present work is of order 150 nm. An angular (orientation) resolution of order 0.05° has been achieved with pattern matching to dynamical simulations as described in [36].

3. Light emission: cathodoluminescence (CL) hyperspectral imaging

The absorption of energetic electrons in a semiconductor results in the generation of excess charge carriers, and the radiative recombination of these carriers results in the phenomenon of cathodoluminescence (CL) [16]. The material's intrinsic luminescence properties are influenced by crystal structure, composition and strain, while additional bands are introduced by defects. While comparable techniques (photoluminescence, electroluminescence) also reveal such information, the higher spatial resolution of CL allows further data to be obtained, such as the mapping of individual extended defects which produce dark features due to non-radiative recombination [41, 42]. The spatial resolution of CL imaging is strongly dependent on the excitation volume (which depends on incident beam energy), the diffusion length of the material and the structure under investigation (e.g. bulk material versus nanostructures). If the material under investigation contains structures which can localise the carriers, such as quantum wells or defects, the spatial resolution can be of the order of 10 nm [43, 44]. In this work, all CL data were acquired at an electron beam energy of 5 keV, which has an excitation volume with a diameter of order 100 nm. Extending the technique beyond simple intensity imaging and into the *hyperspectral imaging* mode allows the technique to be used to map energy shifts and peak widths, and to deconvolve overlapping spectral peaks [45]. The spectral resolution is defined by the spectrometer used, the

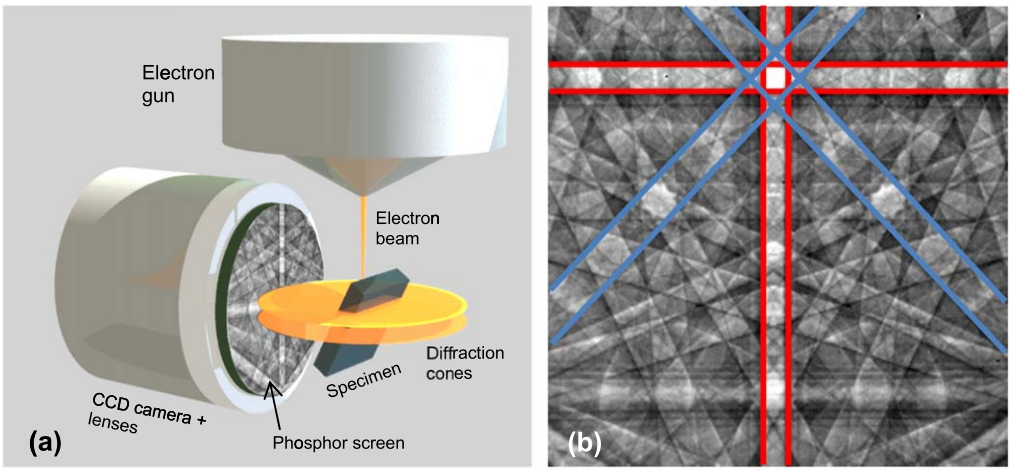

Figure 3. (a) Illustration of the EBSD detection geometry and a conventional EBSD detector, (b) An EBSP from Si acquired at an energy of 20 keV with a collection angle of ≈50°. The red lines (the horizontal and vertical lines) outline Kikuchi bands corresponding to {200} planes, the blue lines (the diagonal lines) outline Kikuchi bands corresponding to {220} planes. Reproduced from [33]. CC BY 3.0.

ruling of the grating and the slit width. For the results presented in this paper, the spectral resolution was typically better than 2 nm. Moreover, CL is not limited to the visible spectrum, but can be used in the deep UV. A particular advantage of the technique when working with UV materials, such as AlN (room temperature band gap ≈ 6 eV) and AlGaN (room temperature band gap ranges from the band gap of GaN of ≈ 3.4 eV to that of AlN), is that it does not require an above-bandgap optical excitation source. The additional challenge of working with such higher resistivity materials under an electron beam has been successfully met through the use of variable chamber pressures to dissipate charge [46], as discussed at the end of section 1.

4. Results

4.1. ECCI of a c-plane $Al_{0.28}Ga_{0.72}N$ thin film

Figure 4 shows an ECCI micrograph of an $Al_{0.28}Ga_{0.72}N/GaN$ thin film grown by metalorganic vapour phase epitaxy (MOVPE). More details on the sample structure and growth can be found in [47]. The ECCI micrograph was acquired at an electron beam energy of 30 keV using the Sirion SEM. The variation in grey scale in the image is a result of different orientations in the film, revealing sub-grains in the thin film. The 'spots' in the image, most of which exhibit a black-white contrast (B-W) (see inset of figure 4), are TDs propagating to the surface of the sample and are revealed due to associated strain fields [48]. A large number of the TDs are seen to lie on sub-grain boundaries. Note that in order to reveal all misorientations, and thus all the sub-grain boundaries, a number of ECCI micrographs need to be acquired under a range of diffraction conditions [49]. While the contrast in the ECCI micrograph reveals the presence of sub-grains, it does not provide any quantitative information on their orientation. The magnitude and direction of misorientation can be measured by EBSD, and an EBSD study of sub-grain orientations are presented, in the next section 4.2, for an AlN thin film.

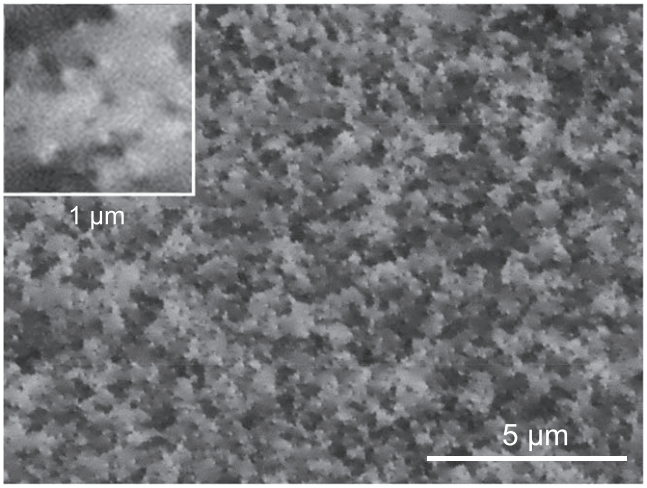

Figure 4. ECCI micrograph from AlGaN thin film. Inset shows dislocation 'spots' at higher magnification. Reproduced from [50]. CC BY 4.0.

Techniques have also been developed to identify dislocation types [9, 21, 51]. Nitride semiconductors contain three types of TDs, namely screw-, edge- and mixed-type dislocations. To identify the TD type, it is possible to apply the 'invisibility criteria' used in transmission electron microscopy (TEM) [9]. In simple terms, dislocations are invisible in an ECCI or TEM micrograph if they do not distort the plane(s) which diffract the incident electron beam. The invisibility criteria are satisfied for screw dislocations where $\boldsymbol{g}\cdot\boldsymbol{b} = 0$ and for edge and mixed dislocations where $\boldsymbol{g}\cdot\boldsymbol{b} = 0$ and $\boldsymbol{g}\cdot(\boldsymbol{b}\times\boldsymbol{u}) = 0$. Where $\boldsymbol{g}$ is the **g**-vector, i.e. the normal to the diffracting plane as discussed in section 2.2, $\boldsymbol{b}$ is the Burgers vector of the TD and $\boldsymbol{u}$ is its line direction. For ECCI, to determine $\boldsymbol{g}$ the acquisition of an ECP pattern (as described in section 2.2) is usually required [9]. However, a further factor which needs to be taken into account when attempting to apply the invisibility criteria to ECCI images (and plan view TEM images), is the effect of surface relaxation on the

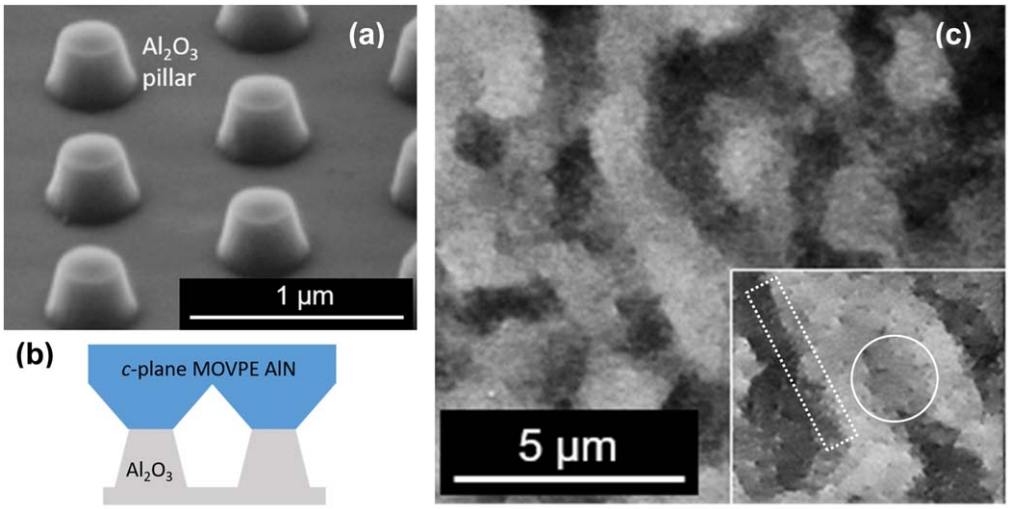

Figure 5. (a) Secondary electron image of nPSS, (b) schematic of overgrowth of AlN on nPSS and (c) ECCI micrograph from an AlN thin film, inset is on same scale but with higher resolution. Reproduced from [50]. CC BY 4.0.

observed defect contrast. The variation in strain due to surface relaxation around a defect can dominate the observed defect contrast [9]. For nitride semiconductor thin films, surface relaxation has a major impact on the observed TD contrast, so additional strategies have been developed to identify the TDs. As discussed above, in an ECCI micrograph TDs appear as spots exhibiting B–W contrast. If two (or more) ECCI micrographs of the same area are acquired at different diffraction conditions, the direction of the B–W contrast exhibited for each TD may be compared. If the B–W contrast direction for a given TD remains the same or is reversed, the TD is an edge dislocation. If the B–W contrast direction changes its direction by other than 0° or 180°, then the dislocation contains a screw component so it is a screw or mixed TD. One advantage of this latter strategy is that it can be applied without a precise knowledge of $\boldsymbol{g}$.

For this AlGaN/GaN thin film the average TD density was determined to be $\approx 3 \times 10^9$ cm^{-2}. Approximately two thirds of the total TDs were found to be edge-type TDs by comparing the B–W contrast direction of the TDs for ECCI micrographs acquired under multiple diffraction conditions.

4.2. ECCI and EBSD mapping of a c-plane AlN thin film overgrown on a nano-patterned sapphire substrate (AlN/nPSS)

Figure 5 shows ECCI micrographs from a ≈7 μm thick *c*-plane AlN thin film overgrown by MOVPE on a nano-patterned sapphire substrate (nPSS). For this sample the sapphire substrate has a 0.1° offcut towards the sapphire *m*-plane. A hexagonal array of truncated cones was prepared on a 2 inch wafer by combining displacement Talbot lithography and lift-off to create a metal nanodot mask, followed by chlorine-based dry etching [52, 53]. AlN was overgrown according to the growth process given in [54, 55].

The motivation for the growth of AlN on nPSS is to produce high quality (low dislocation density) AlN/sapphire templates for the manufacture of high performance UV LEDs. The reduction of dislocation densities from $\approx 1 \times 10^{10}$ to $\approx 5 \times 10^8$ cm^{-2} has been shown to improve the IQE of UV LED structures from ≈5% to ≈ 40% [56].

Figure 5(a) shows a secondary electron image of the nPSS and figure 5(b) shows a schematic of the cross-section of the desired AlN overgrowth. The ECCI micrographs shown in figure 5(c) of the AlN/nPSS were acquired at an electron beam energy of 25 keV using the Quanta SEM operated in low vacuum mode (0.5 mbar) to avoid charging of this insulating specimen.

The variation in greyscale in the ECCI micrograph of figure 5(c) is a result of small differences in orientation of sub-grains in the thin film. The inset (same scale) shows a higher resolution ECCI micrograph where TDs propagating to the surface of the sample are also revealed. A significant number of the TDs are located on the sub-grain boundaries—one of the more obvious sub-grain boundaries is highlighted by the dashed box on the left of the inset in figure 5(c). The TDs which line up along this sub-grain boundary all exhibit the same direction of black-white contrast (perpendicular to the sub-grain boundary), this is consistent with them being edge dislocations aligned along a low angle grain boundary [57]. Careful inspection of the sub-grain exhibiting bright contrast in the centre of the inset image reveals that it contains regions exhibiting different contrast, the region highlighted by the circle is a further sub-grain surrounded by dislocations. The black-white contrast for some of the dislocations surrounding this sub-grain is harder to determine, but for those dislocations showing sufficient contrast, the black-white contrast is also perpendicular to the sub-grain boundary. Acquiring ECCI micrographs over a range of diffraction conditions changes both the sub-grain and dislocation contrast enabling a more thorough analysis of the dislocations and their relationship to the sub-grains, see for example [20, 58].

For this sample the average TD density was determined to be $\approx 1.5 \times 10^9$ cm^{-2}. Approximately 90% of the TDs were found to be edge-type TDs on comparing the B–W contrast direction of the TDs for ECCI micrographs acquired under multiple diffraction conditions.

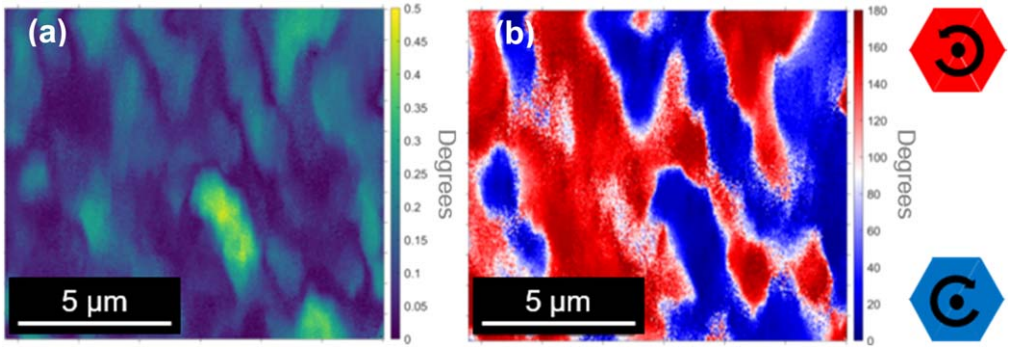

Figure 6. EBSD maps from the AlN/nPSS thin film (a) grain reference orientation deviation (GROD) map and (b) GROD axis map relative to the sample normal (*c*-axis, [0001] direction]) where the colours denote direction of in-plane rotation (i.e. around the *c*-axis). The red regions are rotated in the opposite direction to the blue regions as indicated. Reproduced from [50]. CC BY 4.0.

As discussed in the previous section, while ECCI reveals misorientations between sub-grains, it does not provide a measure of the magnitudes and directions of the misorientations. To obtain quantitative information, EBSD data were acquired from the same sample at an electron beam energy of 20 keV using the Quanta SEM again in low vacuum mode. Figure 6(a) shows a grain reference orientation deviation (GROD) map (the deviation of orientation of the sub-grains relative to an average orientation [59]) derived from EBSD data using MTEX [60]. The first step of the analysis involved comparison of each EBSP with a dynamically simulated pattern [61]. Figure 6(b) is a GROD angle map which shows the local misorientations relative to the normal to the sample, i.e. the *c*-axis ([0001] direction) and reveals that the local misorientations are predominantly rotations around the *c*-axis. As shown schematically in figure 6(b), the colours, blue and red, denote the direction of in-plane rotation. The red regions are rotated in the opposite direction to the blue regions. Work is ongoing to determine the origin of the observed sub-grain rotations, but it is most likely related to the mismatch between the AlN layer and its substrate. 3-D islands form in the early stages of growth, strain relaxation of these islands may result through the introduction of 60° misfit dislocations. These misfit dislocations may induce in-plane misorientations of the islands [62].

These results illustrate how ECCI and EBSD can provide complementary structural information. ECCI allows fast determination of dislocation densities and their distribution and reveals the presence of sub-grains. The ECCI micrographs of figure 5(c) took around 10 min of direct acquisition. EBSD provides quantitative information on the magnitude and direction of the misorientations in the film. However, the EBSD data from which the maps of figure 6 were derived, took of order three hours to acquire. The EBSD data acquisition was then followed by further data analysis which is also time consuming. The time required to acquire the EBSD data can result in drift and in this case a number of datasets were acquired before one was obtained which was relatively drift free. Note that a slight drift can be seen within the top micron of the maps shown in figure 6. In spite of this, both techniques share the advantages of being non-destructive and can be used to interrogate large areas of a sample.

4.3. CL imaging and ECCI of a semi-polar (11-22) GaN thin film overgrown on GaN microrods on m-sapphire

UV LEDs produced from semi-polar nitride semiconductor thin films promise higher performance than those produced from their polar counterparts, due to reduction of piezoelectric and spontaneous polarisation fields. Unfortunately, semi-polar nitride semiconductor thin films are often of poor quality with a high density of structural defects; in particular basal-plane stacking faults, in addition to TDs [62–66]. Here we report the study of the structural and luminescence properties of a 5 μm thick (11–22) GaN epilayer overgrown by MOVPE on a regular array of microrods on an *m*-plane sapphire substrate using ECCI and room temperature CL imaging. The microrod template and overgrowth are designed to reduce the density of structural defects through overgrowth initiated from the sidewalls of the microrods and exploitation of the faster growth rate in the *c*-direction compared to the *a*- and *m*-plane directions to block the propagation of defects, for more information see [65]. Figure 7(a) shows a schematic of the structure and illustrates that the growth gives rise to alternating striped regions, where basal-plane stacking faults reach the surface of the sample or are basal-plane stacking fault free, respectively. Figures 7(b) and (d) show an ECCI micrograph and integrated CL intensity image of the GaN near band edge (NBE) emission (3.15–3.50 eV), respectively. These images are plotted on the same scale but were not obtained from the same part of the semi-polar sample. The ECCI micrograph was acquired at an electron beam energy of 30 keV in the Sirion SEM while the CL image was acquired at an electron beam energy of 5 keV. The ECCI micrograph of figure 7(b) reveals that the GaN thin film does indeed exhibit striped regions of high basal-plane stacking fault density separated by regions with almost no basal-plane stacking faults. For more information on basal-plane stacking faults in semi-polar GaN thin films see [65, 67, 68]. The average basal-plane stacking fault density in the high basal-plane stacking fault density regions is estimated to be of order 1×10^5 cm^{-1}. The NBE CL image of figure 7(d) shows alternating bright and dark stripes, we attribute the significant reduction in the NBE luminescence intensity in the dark striped regions to non-radiative recombination (at room temperature) at the basal-plane stacking faults. Figure 7(c) shows example CL spectra from a bright stripe and from a dark stripe, respectively, (the boxes on

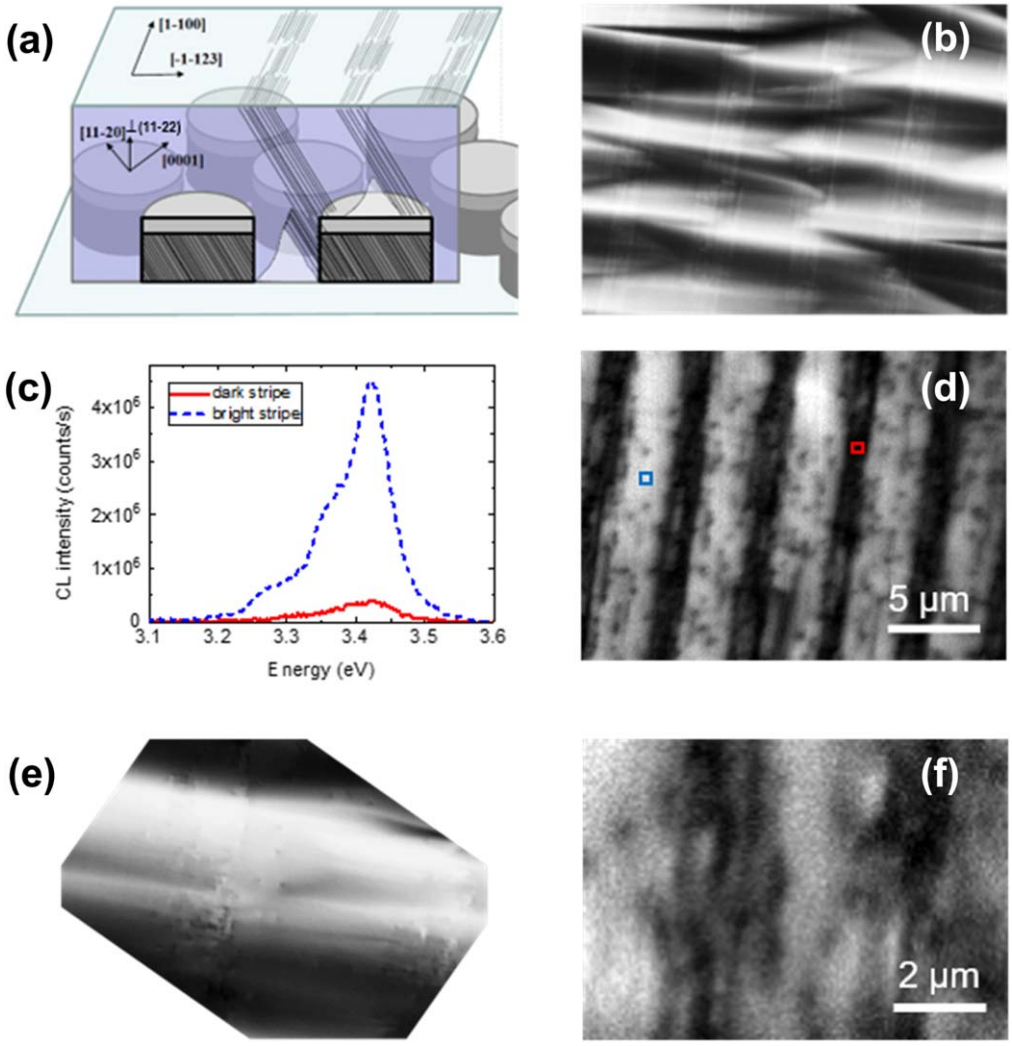

Figure 7. (a) Schematic of semi-polar GaN microrod template and overgrowth, indicating the distribution of stacking faults on the surface of the sample and the crystallographic directions. (b) ECCI micrograph revealing basal-plane stacking faults. (c) Example room temperature CL spectra from a dark stripe and a bright stripe, respectively. The boxes on figure 7(d) indicate where the spectra were extracted from the CL dataset. (d) Integrated CL intensity image of the GaN near band edge (NBE) emission (3.15–3.50 eV) on the same scale as (b) but not from the same area. (e) Higher resolution ECCI micrograph revealing dislocations. (f) Integrated CL intensity image of the GaN near band edge (NBE) emission (3.15–3.50 eV) on the same scale as (e) but not from the same area. Reproduced from [50]. CC BY 4.0.

figure 7(d) indicate where the spectra were extracted from the CL dataset) and show that the peak intensity of the NBE peak drops by around an order of magnitude in the dark striped regions compared to the bright striped regions. At low temperature, distinctive luminescence peaks associated with basal-plane stacking faults are generally observed [69–71]. However, the intensities of these peaks reduce significantly as the temperature is increased and are difficult to resolve from the broad free exciton peak at room temperature. As our CL maps have been acquired at room temperature, the dominant effect of the presence of stacking faults is a reduction in luminescence intensity.

Figures 7(e) and (f) show a higher magnification ECCI micrograph and a higher magnification CL map respectively (same scale, not the same part of the sample). This ECCI micrograph reveals striped regions with alternating higher and lower dislocation densities. By changing the tilt and rotation of the sample, diffraction conditions can be selected to provide the strongest contrast for the stacking faults or for the dislocations.

The dislocation density in the high density regions is $\approx 2 \times 10^9$ cm^{-2}, while for the lower density region it is $\approx 2 \times 10^8$ cm^{-2} [67]. We attribute the black spots in the CL images of figures 7(d) and (f) to non-radiative recombination at single or clusters of dislocations.

In summary, comparison of the ECCI micrographs with the CL images show, that at room temperature, both basal-plane stacking faults and dislocations lead to a significant reduction in the NBE luminescence intensity due to non-radiative recombination at these defects.

4.4. ECCI and CL hyperspectral imaging of a c-plane Si-doped $Al_{0.82}Ga_{0.18}N$ thin film grown on a stripe patterned epitaxially laterally overgrown (ELO) AlN/sapphire template

The topography, type and distribution of dislocations, and light emission were investigated for a polar (*c*-plane) Si-doped $Al_{0.82}Ga_{0.18}N$ thin film grown on a stripe patterned ELO

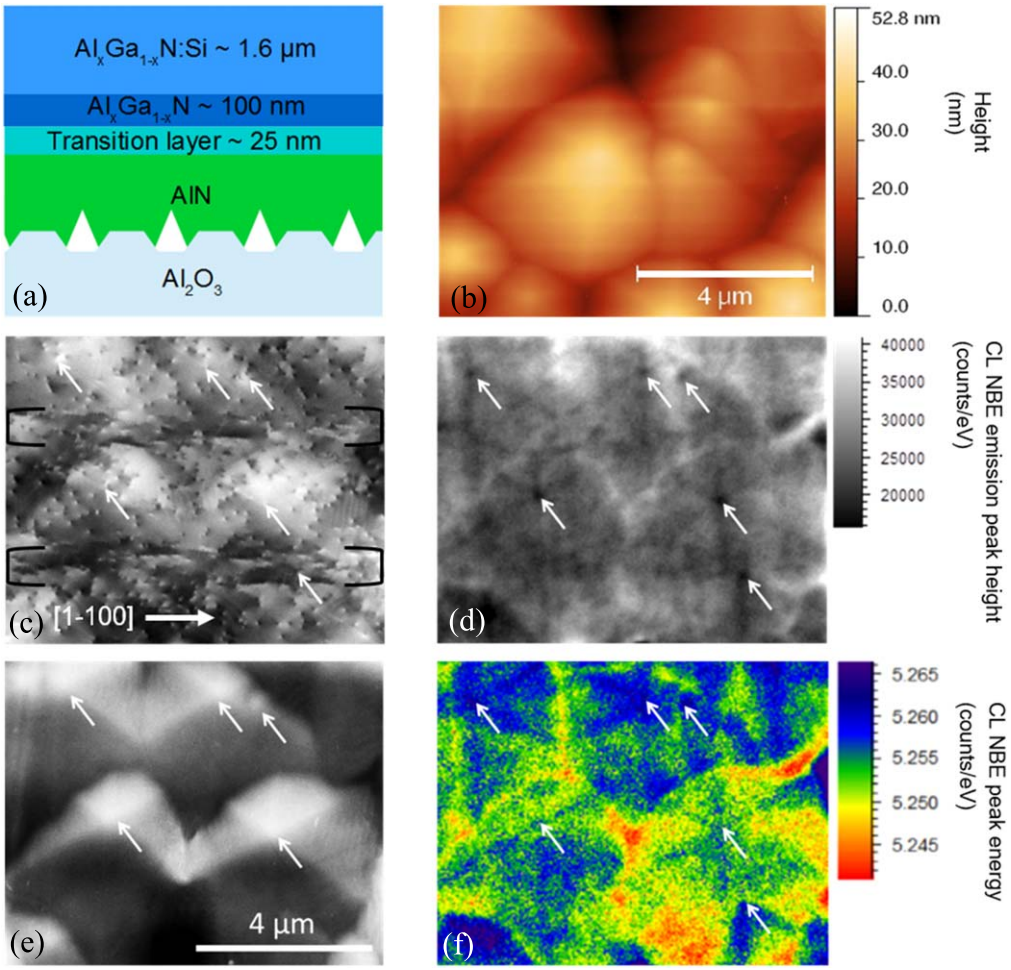

Figure 8. (a) Schematic of the sample structure. x is nominally 0.8, but was measured to be 0.82 for the top 1.6 μm layer. (b) Atomic force microscopy image of the sample surface. (c) ECCI micrograph (the black brackets indicate 'stripes' of higher dislocation density in the coalescence region). (d) CL near band edge (NBE) peak intensity map. (e) Topographic image (f) NBE CL peak energy map. Images (c)–(f) where acquired from approximately the same region of the sample. The white arrows indicate the apexes of the hillocks. The CL peak intensity and peak energy were extracted from hyperspectral data. Reproduced from [50]. CC BY 4.0.

AlN/sapphire template [41]. Both the template and thin film were grown by MOVPE. The stripe pattern comprised 2 μm wide stripes (seed regions), separated by 1 μm wide grooves (window regions), running perpendicular to the substrate miscut of ≈0.25° towards the sapphire *m*-plane (1-100). Note that the sapphire *m*-plane is perpendicular to AlN *m*-plane so that the stripes run parallel to the [1-100] direction for the ELO AlN and for any subsequently grown nitride layers. More details on the template growth can be found in [72]. For the sample we report on here, the template was overgrown by a 400 nm thick AlN buffer layer followed by a 25 nm thick $Al_xGa_{1-x}N$ graded transition layer and a 100 nm thick non-intentionally doped $Al_{0.8}Ga_{0.2}N$ layer. Finally, a 1600 nm thick Si-doped $Al_{0.82}Ga_{0.18}N$ layer was grown. The average percentage of AlN was determined to be (82 ± 1)% by high resolution x-ray diffraction and wavelength dispersive X-ray (WDX) and the Si-dopant concentration was estimated by WDX to be ≈9 × 10^{18} cm^{-3} [41].

Figure 8(a) shows a schematic of the sample structure. Figure 8(b) is an atomic force microscopy image of the sample, revealing the hillock morphology of the sample. Figure 8(c) is an ECCI micrograph and figure 8(e) is a backscattered electron topographic image; a small rotation of the sample from the orientation at which the ECCI micrograph was acquired results in topographic rather than diffraction contrast dominating the backscattered electron image, so revealing the hillock morphology of the sample. Figure 8(d) is a CL peak intensity image of the AlGaN NBE emission (≈5.24–5.27 eV) and figure 8(f) is a CL peak energy image of the AlGaN NBE emission. The ECCI micrograph and topographic image were acquired at an energy of 30 keV in the Sirion SEM, while the room temperature CL maps were acquired at an energy of 5 keV using the Quanta SEM. As these samples were conducting as a result of the silicon doping, both types of measurements could be made in the standard high vacuum mode. For a detailed discussion of the CL spectroscopy of this sample see [34]. Images in figures 8(c)–(f) were obtained from approximately the same region of the sample. The white arrows indicate the apexes of the hillocks. Complete alignment of these images was not possible as the images were acquired at different sample tilts and rotations. The sample was tilted at 70° from the incident electron beam direction for the ECCI and backscattered

electron topographic image, with a small rotation between the ECCI and topographic images, and it was tilted at 45° for the CL images.

The ECCI micrograph reveals that the patterned template leads to a modulation of the dislocation density with higher dislocation densities around the ELO coalescence boundaries. Analysis reveals an average TD density of $\approx 1.2 \times 10^9$ cm^{-2}, with a density of $\approx 2.3 \times 10^9$ cm^{-2} around the coalescence boundaries and a dislocation density of $\approx 1.0 \times 10^9$ cm^{-2} in the lower dislocation regions. 97% of the dislocations were found to be edge-type dislocations. High resolution ECCI micrographs (not shown here) show that the dislocations at the coalescence boundaries are arranged in lines with the same direction of black-white contrast (perpendicular to the coalescence boundary), in a similar manner to the rotation boundaries observed for the AlN thin film described in section 4.2. This observation is consistent with coalescence giving rise to low-angle grain boundaries.

Comparison of the ECCI micrograph of figure 8(c) and the topographic image of figure 8(e) shows that TDs with a screw component are located at the apex of each hillock. The ECCI micrograph also shows atomic steps around the hillocks. This hillock morphology is a result of spiral growth around the screw component dislocations [73–75].

Comparing the ECCI micrograph with the CL NBE peak intensity image in figure 8(e) reveals that the presence of dislocations leads to a reduction in the luminescence, in particular dislocations with a screw component appear as dark spots in the CL image.

Comparing figures 8(e) and (f) shows that the NBE emission is red-shifted at the edges of the hillocks. The AlGaN peak energy is dependent on the relative percentages of GaN and AlN in the AlGaN thin film, the lower the energy of the NBE emission, the higher the percentage of GaN in the film. The peak position will also be influenced by strain and by doping density.

In summary, in this case topographic, ECCI and CL micrographs were acquired from nominally the same part of a sample, allowing the influence of defects and morphology on the light emission to be directly interrogated.

4.5. EBSD and CL of GaN nanowires to determine polarity and its influence on light emission

GaN structures with the N-polar orientation have several advantages over the commonly used Ga-polarity, but the epitaxial growth of smooth surfaces can be challenging. Reversing the direction of the polarisation fields can be beneficial for optoelectronic devices, in particular transistors, photodetectors, solar cells and tunnel junction diodes [76].

Here we summarise coincident EBSD and CL results obtained from self-induced GaN nanowires (NWs) [40]. The NWs were produced on (111)-orientated Si substrates using a two-step growth using metal-organic chemical vapour deposition. Deposition of Al on the Si substrate first forms Al or Si–Al alloy nanodots, which then act as nucleation sites for the subsequent NW growth. EBSD measurements allowed the polarity of the NWs to be determined, while analysis of CL spectra from NWs of known polarity enabled the influence of polarity on light emission to be investigated. The EBSD data were acquired at an electron beam energy of 20 keV, while the room temperature CL data were acquired at 5 keV.

For EBSD, for the noncentrosymmetric wurtzite structure of GaN, the inequivalence of the Bragg reflections on either side of Kikuchi bands corresponding to polar or semi-polar planes, leads to an asymmetric band profile for such bands. This results in the intensity maximum being slightly shifted from the centre of these Kikuchi bands [77]. This shift in intensity is to opposite sides of the Kikuchi bands for N-polar compared to Ga-polar GaN. A comparison of experimental EBSPs with dynamically simulated EBSPs makes it possible to assign the correct (*hkl*) and (*-h-k-l*) to the Kikuchi band edges and thus determine the direction of the polar *c*-axis in the GaN NWs.

Figure 9(a) shows a backscattered electron image of the area of the sample investigated by EBSD and CL hyperspectral imaging. Figure 9(b) shows a cross-correlation difference map showing N-polarity in blue and Ga-polarity in red, overlaid on a backscattered electron intensity image derived from raw EBSPs. The cross-correlation coefficient is a measure of the agreement between the experimental and simulated patterns [78, 79]. Figure 9(b) reveals that some of the NWs are N-polar and some are Ga-polar. A number of the NWs are also of mixed polarity and will contain inversion domain boundaries as reported in [80, 81].

The polarity of some of the NWs is also indicated with the blue (N-polarity), red (Ga-polarity) and green (mixed polarity) coloured circles on figure 9(a). Example experimental EBSPs from N- and Ga-polarity wires are shown in figures 9(c) and (d) respectively, these were acquired from the NWs marked by the blue and red crosses in figure 9(a). The corresponding simulated patterns are shown in figures 9(e) and (f). The differences between the experimental EBSPs from the N- and Ga- polarity wires are highlighted in the normalised intensity difference of the two experimental patterns in figure 9(g). Figure 9(h) shows the same for the simulated EBSPs. The greatest differences in intensity manifest as 'lines' of blue and red. This is a result of the opposite asymmetries in the intensity distributions for Kikuchi bands corresponding to semi-polar planes for the two polarities, as indicated by the black and white arrows in figure 9(h).

Figure 10 shows room temperature CL spectra from the top surface of the NWs. These were extracted from the CL hyperspectral data set and categorised according to the polarity determined by EBSD. Figures 10(a) and (b) show the CL spectra of the GaN NBE emission for several Ga-polar and N-polar NWs, respectively, normalised to the NBE peak height and offset vertically for clarity. The Ga-polar NWs exhibit a dominant NBE emission at 368 nm, whereas the N-polar NWs emit at 365 nm. This wavelength (energy) shift of 3 nm (30 meV) may be due to several factors. The different growth condition for each polarity can cause changes in overall strain. Different polarities are also known to show changes in impurity incorporation, such as Si-doping, leading to a redshift in the band edge emission of Ga-polar material

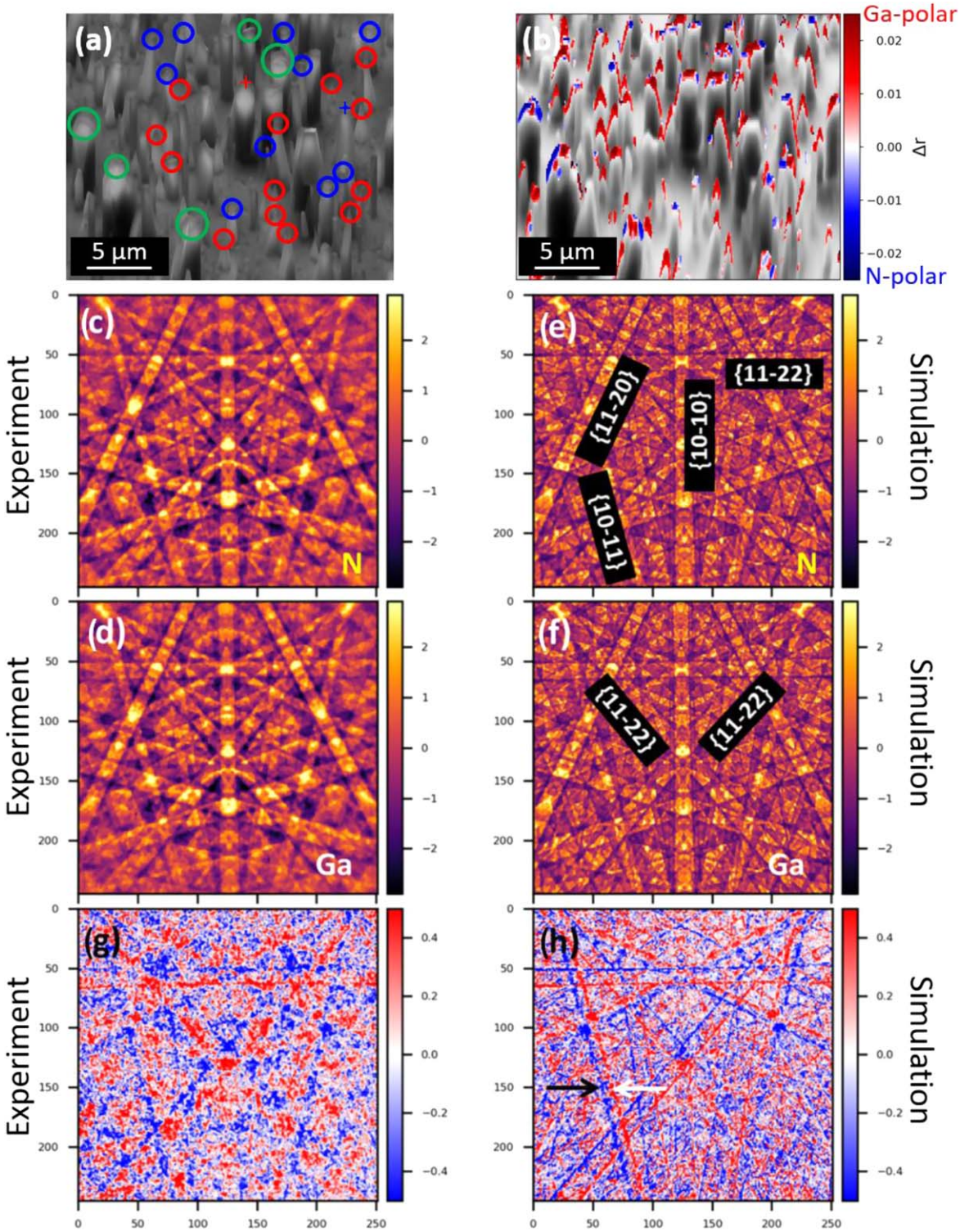

Figure 9. (a) Backscattered electron image of the area of the sample investigated by EBSD. The NWs circled in blue are N-polarity, those circled in red are Ga-polarity and those circled in green are mixed polarity. (b) Cross-correlation difference map indicating N-polarity in blue and Ga-polarity in red, overlaid on a BSE intensity image derived from the raw EBSPs. (c) Experimental EBSP from the point marked with a blue cross from a GaN NW with N-polarity, (d) experimental EBSP from the point marked with a red cross from a GaN NW with Ga-polarity. (e), (f) Simulated patterns for N and Ga-polarity, respectively. (g) Normalised intensity difference image of the experimental EBSPs (from (c) and (d)), and (h) normalised intensity difference image of simulated EBSPs (from (e) and (f)). The white arrow points to {10-11} and the black arrow points to {10-1-1}. Reproduced from [40]. CC BY 4.0.

compared with N-polarity [82, 83]. Figures 10(c) and (d) display the same CL spectra as figures 10(a) and (b) but now normalised to the GaN NBE peak height, without the vertical offset and showing the entire recorded spectral range including the yellow band (YB) emission for Ga-polar and N-polar NWs, respectively. Comparing the YB emission of

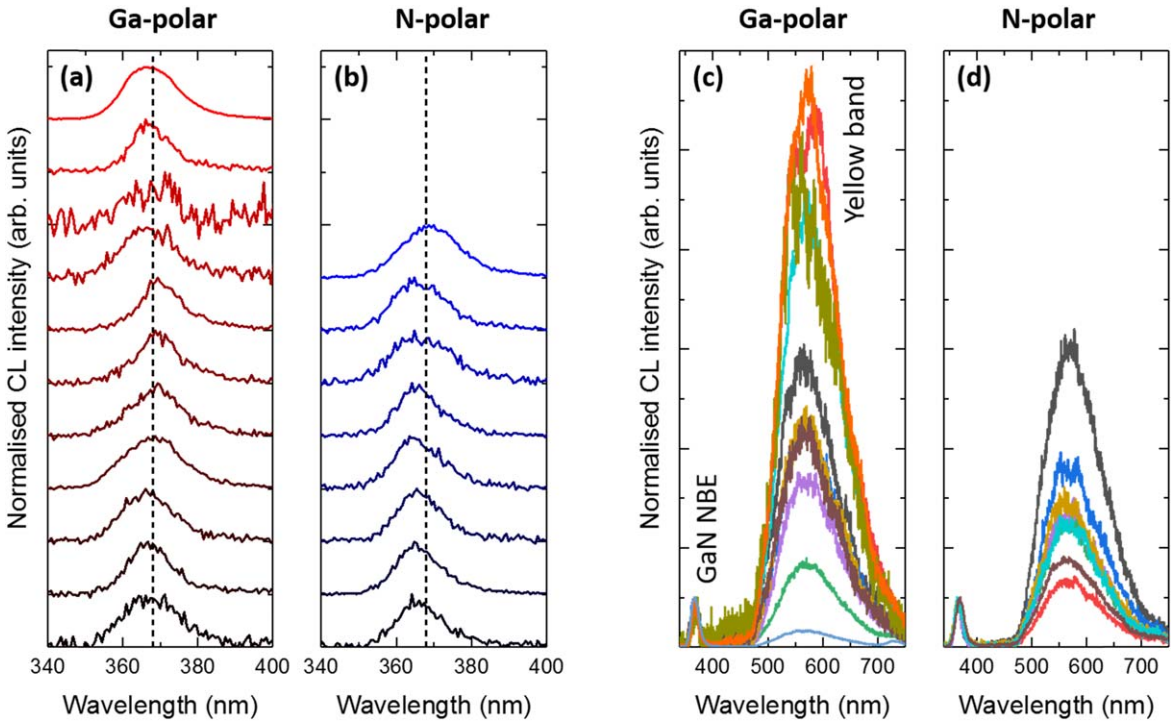

Figure 10. Room temperature CL spectra extracted from a single hyperspectral CL data set, showing the GaN NBE emission for several (a) Ga-polar and (b) N-polar nanowires. The spectra are taken from the top of the nanowires, are normalised to the GaN NBE peak height, and are offset vertically for clarity. The vertical dashed lines show the approximate peak position of the Ga-polar nanowires. (c) and (d) show the same spectra without the offset but for the entire recorded spectral range for the Ga-polar and N-polar nanowires, respectively. Reproduced from [40]. CC BY 4.0.

the set of Ga-polar and N-polar NWs, the N-polar NWs show an overall reduced contribution from the defect-related YB emission which relates to a reduction of defects contributing to this emission [84].

To summarise, by combining EBSD and CL it is possible to determine the polarity of a noncentrosymmetric semiconductor structure on the nanoscale and investigate the influence of polarity on light emission properties. For a discussion of what may determine the polarity of a given NW, see [85] for example. How the NWs nucleate seems to be key to their final polarity. As EBSD and CL are non-destructive techniques, their use to characterise a systematic set of samples grown under different growth conditions maybe one approach to shed more light on why a given rod possesses Ga-, N- or mixed polarity.

5. Summary and conclusions

In summary, we have illustrated the capabilities of the SEM techniques of ECCI, EBSD and CL which can be used to provide complementary information on material properties encompassing topography, structure, composition and light emission down to the nanoscale. Recent general availability of environmental/variable pressure SEMs has also made the characterisation of wide bandgap and therefore resistive materials such as AlN and AlGaN in the SEM far more accessible. We have shown that used together, EBSD and ECCI can provide valuable information on misorientations and on extended defects such as dislocations. If ECCI is combined with CL, the influence of extended defects on light emission can be investigated and if EBSD is combined with CL, the influence of structural properties, such as polarity, on light emission can be determined. In conclusion the SEM is a very powerful tool with which to investigate both structural and light emitting properties of semiconductors.

Acknowledgments

The authors would like to acknowledge financial support of the EPSRC, UK via Grant No. EP/J015792/1, ‘Nanoscale characterisation of nitride semiconductor thin films using EBSD, ECCI, CL and EBIC’; Grant No. EP/M015181/1, ‘Manufacturing nano-engineered III-nitrides’; and Grant No. EP/P015719/1, ‘Quantitative non-destructive nanoscale characterisation of advanced materials’. Work at Ferdinand-Braun-Institute and TU Berlin was partially supported by the German Research Council (DFG) within the CRC 787 (Nanophotonics) and the German Federal Ministry of Research and Education within the Advanced UV for Life project consortium. Data associated with this research are available at https://doi.org/10.15129/b5238863-a088-4f30-8b13-2625260eb73a [50] and https://doi.org/10.15129/b152a121-3495-4235-b9cd-985bf1355cd8 [40].

ORCID iDs

C Trager-Cowan https://orcid.org/0000-0001-8684-7410
J Bruckbauer https://orcid.org/0000-0001-9236-9320
P R Edwards https://orcid.org/0000-0001-7671-7698
R W Martin https://orcid.org/0000-0002-6119-764X
P J Parbrook https://orcid.org/0000-0003-3287-512X
C Kuhn https://orcid.org/0000-0003-1735-6209
P A Shields https://orcid.org/0000-0003-0517-132X
J Bai https://orcid.org/0000-0002-6953-4698
L Jiu https://orcid.org/0000-0001-5014-297X

References

[1] Holt D B and Joy D C 1989 *SEM Microcharacterization of Semiconductors* (New York: Academic)
[2] Goldstein J, Newbury D, Joy D, Lyman C, Echlin P, Lifshin E, Sawyer L and Michael J 2007 *Scanning Electron Microscopy and X-ray Microanalysis* (Berlin: Springer)
[3] Reimer L 1998 *Scanning Electron Microscopy: Physics of Image Formation and Microanalysis* (Berlin: Springer)
[4] Zhou W and Wang Z L 2007 *Scanning Microscopy for Nanotechnology: Techniques and Applications* (New York: Springer)
[5] Wilkinson A J and Hirsch P B 1997 Electron diffraction based techniques in scanning electron microscopy of bulk materials *Micron* **28** 279–308
[6] Trager-Cowan C, Sweeney F, Trimby P W, Day A P, Gholinia A, Schmidt N-H, Parbrook P J, Wilkinson A J and Watson I M 2007 Electron backscatter diffraction and electron channeling contrast imaging of tilt and dislocations in nitride thin films *Phys. Rev.* B **75** 085301
[7] Crimp M A, Simkin B A and Ng B C 2001 Demonstration of the g·bxu = 0 edge dislocation invisibility criterion for electron channelling contrast imaging *Phil. Mag. Lett.* **81** 833–7
[8] Picard Y, Kamaladasa R, De Graef M, Nuhfer N, Mershon W, Owens T, Sedlacek L and Lopour F 2012 Future prospects for defect and strain analysis in the SEM via electron channeling *Micros. Today* **20** 12–6
[9] Naresh-Kumar G, Hourahine B, Edwards P R, Day A P, Winkelmann A, Wilkinson A J, Parbrook P J, England G and Trager-Cowan C 2012 Rapid nondestructive analysis of threading dislocations in wurtzite materials using the scanning electron microscope *Phys. Rev. Lett.* **108** 135503
[10] Zaefferer S and Elhami N N 2014 Theory and application of electron channelling contrast imaging under controlled diffraction conditions *Acta Mater.* **75** 20–50
[11] Deitz J I, Carnevale S D, Ringel S A, McComb D W and Grassman T J 2015 Electron channeling contrast imaging for rapid III–V heteroepitaxial characterization *J. Vis. Exp.* **101** e52745
[12] Naresh-Kumar G, Thomson D, Nouf-Allehiani M, Bruckbauer J, Edwards P R, Hourahine B, Martin R W and Trager-Cowan C 2016 Electron channelling contrast imaging for III-nitride thin film structures *Mater. Sci. Semicond. Process.* **47** 44–50
[13] Schwartz A J, Kumar M, Adams B L and Field D P 2009 *Electron Backscatter Diffraction in Materials Science* (Berlin: Springer)
[14] Wilkinson A J and Britton T B 2012 Strains, planes, and EBSD in materials science *Mater. Today* **15** 366–76
[15] Yacobi B G and Holt D B 1990 *Cathodoluminescence Microscopy of Inorganic Solids* (New York: Plenum)
[16] Edwards P R and Martin R W 2011 Cathodoluminescence nano-characterization of semiconductors *Semicond. Sci. Technol.* **26** 064005
[17] Yakimov E B 2012 Investigation of electrical and optical properties in semiconductor structures via SEM techniques with high spatial resolution *J. Surf. Invest.* **6** 887–9
[18] Kneissl M, Seong T Y, Han J and Amano H 2019 The emergence and prospects of deep-ultraviolet light-emitting diode technologies *Nature Photonics* **13** 233–44
[19] Park J S, Kim J K, Cho J and Seong T Y 2017 Group III-nitride-based ultraviolet light-emitting diodes: ways of increasing external quantum efficiency *ECS J. Solid State Sci. Technol.* **6** Q42
[20] Jablon B M, Mingard K, Winkelmann A, Naresh-Kumar G, Hourahine B and Trager-Cowan C 2020 Subgrain structure and dislocations in WC-Co hard metals revealed by electron channelling contrast imaging *Int. J. Refract. Met.* **87** 105159
[21] Winkelmann A, Jablon B M, Tong V, Cowan C and Mingard K 2020 Improving EBSD precision by orientation refinement with full pattern matching *J. Microsc.* (https://doi.org/10.1111/jmi.12870)
[22] Naresh-Kumar G *et al* 2013 Electron channeling contrast imaging studies of nonpolar nitrides using a scanning electron microscope *Appl. Phys. Lett.* **102** 142103
[23] Carnevale S D, Deitz J I, Carlin J A, Picard Y N, De Graef M, Ringel S A and Grassman T J 2014 Rapid misfit dislocation characterization in heteroepitaxial III–V/Si thin films by electron channeling contrast imaging *Appl. Phys. Lett.* **104** 232111
[24] Hite J K, Mastro M A and Eddy C R Jr 2010 Approach for dislocation free GaN epitaxy *J. Cryst. Growth* **312** 3143–6
[25] Schulze A, Strakos L, Vystavel T, Loo R, Pacco A, Collaert N, Vandervost W and Caymax M 2018 Non-destructive characterization of extended crystalline defects in confined semiconductor device structures *Nanoscale* **10** 7058–66
[26] Callahan P G, Haidet B B, Jung D, Seward G G and Mukherjee K 2018 Direct observation of recombination-enhanced dislocation glide in heteroepitaxial GaAs on silicon *Phys. Rev. Mater.* **2** 081601
[27] Yaung K N, Kirnstoetter S, Faucher J, Gerger A, Lochtefeld A, Barnett A and Minjoo L L 2016 Threading dislocation density characterization in III–V photovoltaic materials by electron channeling contrast imaging *J. Cryst. Growth* **453** 65–70
[28] Joy D C, Newbury D E and Davidson D L 1982 Electron channeling patterns in the scanning electron microscope *J. Appl. Phys.* **53** R81–122
[29] Han H, Hantschel T, Strakos L, Vystavel T, Baryshnikova M, Mols Y, Kunert B, Langer R, Vandervorst W and Caymax M 2020 Application of electron channeling contrast imaging to 3D semiconductor structures through proper detector configurations *Ultramicroscopy* **210** 112928
[30] Naresh-Kumar G, Trager-Cowan C and Mingard K P 2019 Electron channelling contrast imaging in a low voltage scanning electron microscope *Microsc. Microanal.* **25** 504–5
[31] Massabuau F C-P, Bruckbauer J, Trager-Cowan C and Oliver R A 2019 Microscopy of defects in semiconductors *Characterisation and Control of Defects in Semiconductors* ed F Tuomisto (London: IET)
[32] Mansour H, Guyon J, Crimp M A, Gey N, Beausir B and Maloufi A N 2014 Accurate electron channeling contrast analysis of dislocations in fine grained bulk materials *Scr. Mater.* **84** 11–4
[33] Vespucci S, Winkelmann A, Naresh-Kumar G, Mingard K P, Maneuski D, Edwards P R, Day A P, O'Shea V and Trager-Cowan C 2015 Digital direct electron imaging of energy-filtered electron backscatter diffraction patterns *Phys. Rev.* B **92** 205301

[34] Wilkinson A J, Moldovan G, Britton T B, Bewick A, Clough R and Kirkland A I 2013 Direct detection of electron backscatter diffraction patterns *Phys. Rev. Lett.* **111** 065506
[35] Tripathi A and Zaefferer S 2019 On the resolution of EBSD across atomic density and accelerating voltage with a particular focus on the light metal magnesium *Ultramicroscopy* **207** 112828
[36] Nolze G, Jürgens M, Olbricht J and Winkelmann A 2018 Improving the precision of orientation measurements from technical materials via EBSD pattern matching *Acta Mater.* **159** 408–15
[37] Wilkinson A J, Meaden G and Dingley D J 2006 High-resolution elastic strain measurement from electron backscatter diffraction patterns: new levels of sensitivity *Ultramicroscopy* **106** 307–13
[38] Naresh-Kumar G, Vilalta-Clemente A, Jussila H, Winkelmann A, Nolze G, Vespucci S, Nagarajan S, Wilkinson A J and Trager-Cowan C 2017 Quantitative imaging of anti-phase domains by polarity sensitive orientation mapping using electron backscatter diffraction *Sci. Rep.* **7** 10916
[39] Winkelmann A, Nolze G, Himmerlich M, Lebedev V and Reichmann A 2016 Point-group sensitive orientation mapping using EBSD *Proc. 6th Int. Conf. on Recrystallization and Grain Growth* ed E A Holm *et al* (Berlin: Springer) pp 281–6
[40] Naresh-Kumar G, Bruckbauer J, Winkelmann A, Yu X, Hourahine B, Edwards P R, Wang T, Trager-Cowan C and Martin R W 2019 Determining GaN nanowire polarity and its influence on light emission in the scanning electron microscope *Nano Lett.* **19** 3863–70
[41] Kusch G *et al* 2015 Spatial clustering of defect luminescence centers in Si-doped low resistivity $Al_{0.82}Ga_{0.18}N$ *Appl. Phys. Lett.* **107** 072103
[42] Naresh-Kumar G *et al* 2014 Coincident electron channeling and cathodoluminescence studies of threading dislocations in GaN *Microsc. Microanal.* **20** 55–60
[43] Bruckbauer J, Edwards P R, Wang T and Martin R W 2011 High resolution cathodoluminescence hyperspectral imaging of surface features in InGaN/GaN multiple quantum well structures *Appl. Phys. Lett.* **98** 141908
[44] Norman C E 2001 Challenging the spatial resolution limits of CL and EBIC *Solid State Phenom.* **78** 19–28
[45] Christen J, Grundmann M and Bimberg D 1991 Scanning cathodoluminescence microscopy—a unique approach to atomic-scale characterization of heterointerfaces and imaging of semiconductor inhomogeneities *J. Vac. Sci. Technol.* B **9** 2358–68
[46] Kusch G, Li H, Edwards P R, Bruckbauer J, Parbrook P J and Martin R W 2014 Influence of substrate miscut angle on surface morphology and luminescence properties of AlGaN *Appl. Phys. Lett.* **104** 092114
[47] Smith M D, Thomson D, Zubialevich V Z, Li H, Naresh-Kumar G, Trager-Cowan C and Parbrook P J 2017 Nanoscale fissure formation in $Al_xGa_{1-x}N$/GaN heterostructures and their influence on Ohmic contact formation *Phys. Status Solidi* a **214** 1600353
[48] Pascal E, Hourahine B, Naresh-Kumar G, Mingard K and Trager-Cowan C 2018 Dislocation contrast in electron channelling contrast images as projections of strain-like components *Mater. Today: Proc.* **5** 14652–61
[49] Day A P and Quested T E 1999 A comparison of grain imaging and measurement using horizontal orientation and colour orientation contrast imaging, electron backscatter pattern and optical methods *J. Microsc.* **195** 186–96
[50] Trager-Cowan C *et al* 2019 Scanning electron microscope as a flexible tool for investigating the properties of UV-emitting nitride semiconductor thin films *Photon. Res.* **7** B73–82
[51] Kamaladasa R J, Liu F, Porter L M, Davis R F, Koleske D D, Mulholland G, Jones K A and Picard Y N 2011 Identifying threading dislocations in GaN films and substrates by electron channelling *J. Microsc.* **244** 311–9
[52] Coulon P M, Kusch G, Fletcher P, Chausse P, Martin R W and Shields P 2018 Hybrid top-down/bottom-up fabrication of a highly uniform and organized faceted AlN nanorod scaffold *Materials* **11** 1140
[53] Coulon P M *et al* 2019 Displacement Talbot lithography for nano-engineering of III-nitride materials *Microsyst. Nanoeng.* **5** 52
[54] Hagedorn S, Knauer A, Mogilatenko A, Richter E and Weyers M 2016 AlN growth on nano-patterned sapphire: a route for cost efficient pseudo substrates for deep UV LEDs *Phys. Status Solidi* a **213** 3178
[55] Walde S *et al* 2020 AlN overgrowth of nano-pillar-patterned sapphire with different offcut angle by metalorganic vapor phase epitaxy *J. Cryst. Growth* **531** 125343
[56] Kneissl M, Seong T Y, Han J and Amano H 2019 The emergence and prospects of deep-ultraviolet light-emitting diode technologies *Nat. Photon.* **13** 233
[57] Potin V, Ruterana P, Nouet G, Pond R C and Morkoç H 2000 Mosaic growth of GaN on (0001) sapphire: A high-resolution electron microscopy and crystallographic study of threading dislocations from low-angle to high-angle grain boundaries *Phys. Rev.* B **61** 5587
[58] L'hôte G, Lafond C, Steyer P, Deschanel S, Douillard T, Langlois C and Cazottes S 2019 Rotational-electron channeling contrast imaging analysis of dislocation structure in fatigued copper single crystal *Scr. Mater.* **162** 103–7
[59] Wright S I, Nowell M M and Field D P 2011 A review of strain analysis using electron backscatter diffraction *Microsc. Microanal.* **17** 316–29
[60] Bachmann F, Hielscher R and Schaeben H 2010 Texture analysis with MTEX - free and open source software toolbox *Solid State Phenom.* **160** 63–8
[61] Winkelmann A, Trager-Cowan C, Sweeney F, Day A P and Parbrook P J 2007 Many-beam dynamical simulation of electron backscatter diffraction patterns *Ultramicroscopy* **107** 414–21
[62] Mantach R, Vennéguès P, Perez J Z, De Mierry P, Leroux M, Portail M and Feuillet G 2019 Semipolar (10-11) GaN growth on silicon-on-insulator substrates: defect reduction and meltback etching suppression *J. Appl. Phys.* **125** 035703
[63] Leung B, Wang D, Kuo Y S and Han J 2016 Complete orientational access for semipolar GaN devices on sapphire *Phys. Status Solidi* b **253** 188
[64] Scholz F 2012 Semipolar GaN grown on foreign substrates: a review *Semicond. Sci. Technol.* **27** 024002
[65] Zhang Y, Bai J, Hou Y, Yu X, Gong Y, Smith R M and Wang T 2016 Microstructure investigation of semi-polar (11-22) GaN overgrown on differently designed micro-rod array templates *Appl. Phys. Lett.* **109** 241906
[66] Bruckbauer J *et al* 2017 Spatially-resolved optical and structural properties of semi-polar (112−2) $Al_xGa_{1-x}N$ with x up to 0.56 *Sci. Rep.* **7** 10804
[67] Naresh-Kumar G, Thomson D, Zhang Y, Bai J, Jiu L, Yu X, Gong Y P, Smith R M, Wang T and Trager-Cowan C 2018 Imaging basal plane stacking faults and dislocations in (11-22) GaN using electron channelling contrast imaging *J. Appl. Phys.* **124** 065301
[68] Vennéguès P 2012 Defect reduction methods for III-nitride heteroepitaxial films grown along nonpolar and semipolar orientations *Semicond. Sci. Technol.* **27** 024004
[69] Paskov P P, Schifano R, Monemar B, Paskova T, Figge S and Hommel D 2005 Emission properties of a-plane GaN grown by metal-organic chemical-vapor deposition *J. Appl. Phys.* **98** 093519
[70] Korona K P, Reszka A, Sobanska M, Perkowska P S, Wysmołek A, Klosek K and Zytkiewicz Z R 2014 Dynamics

of stacking faults luminescence in GaN/Si nanowires *J. Lumin.* **155** 293–7
[71] Lähnemann J, Jahn U, Brandt O, Flissikowski T, Dogan P and Grahn H T 2014 Luminescence associated with stacking faults in GaN *J. Phys. D: Appl. Phys.* **47** 423001
[72] Mogilatenko A, Küller V, Knauer A, Jeschke J, Zeimer U, Weyers M and Tränkle G 2014 Defect analysis in AlGaN layers on AlN templates obtained by epitaxial lateral overgrowth *J. Cryst. Growth* **402** 222–9
[73] Bryan I, Bryan Z, Mita S, Rice A, Hussey L, Shelton C, Tweedie J, Maria J P, Collazo R and Sitar Z 2016 The role of surface kinetics on composition and quality of AlGaN *J. Cryst. Growth* **451** 65–71
[74] Bryan I, Bryan Z, Mita S, Rice A, Tweedie J, Collazo R and Sitar Z 2016 Surface kinetics in AlN growth: a universal model for the control of surface morphology in III-nitrides *J. Cryst. Growth* **438** 81–9
[75] Schade L, Wernicke T, Raß J, Ploch S, Weyers M, Kneissl M and Schwarz U T 2014 Surface topology caused by dislocations in polar, semipolar, and nonpolar InGaN/GaN heterostructures *Phys. Status Solidi* a **211** 756–60
[76] Keller S *et al* 2014 Recent progress in metal-organic chemical vapor deposition of N-polar group-III nitrides *Semicond. Sci. Technol.* **29** 113001
[77] Winkelmann A and Nolze G 2015 Point-group sensitive orientation mapping of non-centrosymmetric crystals *Appl. Phys. Lett.* **106** 072101
[78] Gonzalez R C and Woods R E 1992 *Digital Image Processing* 2nd edn (Boston: Addison-Wesley Longman Publishing Co., Inc.)
[79] Nolze G, Hielscher R and Winkelmann A 2017 Electron backscatter diffraction beyond the mainstream *Cryst. Res. Technol.* **52** 1600252
[80] Labat S *et al* 2015 Inversion domain boundaries in GaN wires revealed by coherent Bragg imaging *ACS Nano* **9** 9210–6
[81] Mkhoyan K A, Batson P E, Cha J, Schaff W J and Silcox J 2006 Direct determination of local lattice polarity in crystals *Science* **312** 1354
[82] Prystawko P, Leszczynski M, Beaumont B, Gibart P, Frayssinet E, Knap W, Wisniewski P, Bockowski M, Suski T and Porowski S 1998 Doping of homoepitaxial GaN layers *Phys. Status Solidi* b **210** 437–43
[83] Salomon D, Messanvi A, Eymery J and Martinez-Criado O 2017 Silane-Induced N-polarity in wires probed by a synchrotron nanobeam *Nano Lett.* **17** 946–52
[84] Li S, Mo C, Wang L, Xiong C, Peng X, Jiang F, Deng Z and Gong D 2001 The influence of Si-doping to the growth rate and yellow luminescence of GaN grown by MOCVD *J. Lumin.* **93** 321–6
[85] Alloing B, Vézian S, Totterea O, Vennéguès P, Beraudo E and Zuniga-Perez J 2011 On the polarity of GaN micro-and nanowires epitaxially grown on sapphire (0001) and Si (111) substrates by metal organic vapor phase epitaxy and ammonia-molecular beam epitaxy *Appl. Phys. Lett.* **98** 011914
[86] Mante N, Rennesson S, Frayssinet E, Largeau L, Semond F, Rouviere J L, Feuillet G and Vennéguès P 2018 Proposition of a model elucidating the AlN-on-Si (111) microstructure *J. Appl. Phys.* **123** 215701